Multi-resolution X-ray phase-contrast and dark-field tomography of human cerebellum with near-field speckles

Sara Savatović,[1,2,*] **Marie-Christine Zdora,**[3,4] **Fabio De Marco,**[1,2] **Christos Bikis,**[5,6] **Margie Olbinado,**[4] **Alexander Rack,**[7] **Bert Müller,**[6] **Pierre Thibault,**[1,2] **and Irene Zanette**[2]

[1]*Department of Physics, University of Trieste, Via Valerio 2, 34127 Trieste, Italy*
[2]*Elettra-Sincrotrone Trieste, Strada Statale 14 – km 163.5, 34149 Basovizza, Italy*
[3]*Department of Biomedical Engineering, ETH Zürich, Gloriastrasse 35, 8092 Zürich, Switzerland*
[4]*Paul Scherrer Institut, Forschungsstrasse 111, 5232 Villigen PSI, Switzerland*
[5]*Psychiatric Hospital in Winterthur, Wieshofstrasse 102, 8408 Winterthur, Switzerland*
[6]*Biomaterials Science Center, Department of Biomedical Engineering, University of Basel, Hegenheimermattweg 167 B/C, 4123 Allschwil, Switzerland*
[7]*ESRF – The European Synchrotron, CS40220, CEDEX 09, 38043 Grenoble, France*
*sara.savatovic@phd.units.it

Abstract: In this study, we use synchrotron-based multi-modal X-ray tomography to examine human cerebellar tissue in three dimensions at two levels of spatial resolution (2.3 µm and 11.9 µm). We show that speckle-based imaging (SBI) produces results that are comparable to propagation-based imaging (PBI), a well-established phase-sensitive imaging method. The different SBI signals provide complementary information, which improves tissue differentiation. In particular, the dark-field signal aids in distinguishing tissues with similar average electron density but different microstructural variations. The setup's high resolution and the imaging technique's excellent phase sensitivity enabled the identification of different cellular layers and additionally, different cell types within these layers. We also correlated this high-resolution phase-contrast information with measured dark-field signal levels. These findings demonstrate the viability of SBI and the potential benefit of the dark-field modality for virtual histology of brain tissue.

1. Introduction

Three-dimensional visualization of the cytoarchitecture of human cerebellar and brain tissue can reveal morphological and cellular alterations, which may be associated with neurological diseases. Variations in cell density or size can be observed in conditions such as essential tremor [1,2], autism [3,4], Parkinson's disease [5] and Alzheimer's disease [6].

X-ray microtomography can be used to image brain tissue [7] while avoiding potential sample damage caused by other standard characterization methods such as histology and electron microscopy [8,9]. However, conventional absorption-based X-ray imaging of unstained samples often fails to provide sufficient contrast between the different types of tissue [10]. X-ray phase-contrast methods have been developed in the last decades to address this challenge [11–14]. In addition to absorption and phase-contrast images, many recent techniques can produce ultra-small angle scattering maps – commonly called dark-field. When available, the dark-field signal can provide information about the unresolved structure and organization of the sample's features [15–18].

As X-rays pass through a medium, they can be absorbed, refracted, or scattered, encoding distinct physical and chemical properties of the tissue under investigation. Multi-modal X-ray imaging methods can access this complementary information through different imaging channels retrieved from the same data set – attenuation, phase contrast, and dark field. These multi-modal X-ray imaging methods include analyzer-based imaging (ABI) [19,20], grating-based imaging (GBI) [21], edge illumination (EI) [22] and, more recently, speckle-based imaging (SBI) [23–25].

High-resolution, high-sensitivity three-dimensional virtual histology of the human cerebellum with X-ray phase-contrast imaging was first reported in 2010 by Schulz et al. [26,27] using GBI. Because of the good contrast, different regions of the cerebellum (white and gray matter) could be easily distinguished. Moreover, with an estimated spatial resolution of 40 µm, it was possible to detect the presence of large neurons called Purkinje cells. While the GBI results shown in [10,26,27] are of high phase sensitivity, the spatial resolution achievable with X-ray grating interferometry is inherently limited by the period of the gratings used in the setup and cannot reach values below a few micrometers due to constraints in the nanofabrication of these devices. Furthermore, the setup lacks flexibility because inter-grating distances cannot be varied independently of photon energies for a given set of gratings. Nonetheless, for a given energy, there are usually several working distances. Propagation-based X-ray phase-contrast imaging (PBI) techniques can deliver results at a higher resolution [28–30]. Micrometer-sized subcellular structures and cell density analysis from single-distance PBI are shown in [31], whereas quantitative nanometer-resolution results were obtained with holotomography in [32]. However, single-distance PBI lacks the capability to retrieve quantitative electron density values, and holotomography requires multiple distances and elaborate reconstruction methods, including volume co-registration.

Consequently, there is a need for a more flexible experimental setup that can facilitate access to multiple imaging channels, while allowing a wide range of spatial resolutions and photon energies. When a randomly-structured membrane (such as sandpaper) is introduced into a sufficiently coherent wave field, self-interference of the disturbed wavefronts generates "speckled", random intensity modulations. SBI uses these intensity modulations as a wavefront marker to decouple the different X-ray interaction mechanisms. A number of different algorithmic methods have been developed for extracting this information from X-ray speckle image data. Most methods use a speckle-tracking approach [23,33–35] derived from digital image correlation techniques [36], while others use an implicit tracking approach [37–40].

Like GBI and EI, speckle-based imaging methods retrieve differential-phase information, i.e., they encode the refraction angles of X-rays within the sample. When combined with tomographic imaging, this information can be used to extract the three-dimensional distribution of electron density [41]. PBI, on the other hand, encodes a different quantity, related to second spatial derivatives of wavefront phase [42]. While the extraction of quantitative information is also possible with holotomography, it requires combining acquisition data from multiple propagation distances [12,32], which is experimentally challenging.

Thus, speckle-based imaging combines the ability to retrieve electron-density distributions quantitatively, while also being able to achieve a high spatial resolution on the order of 1 µm (up to 2.3 µm in this study), and achieves this with a simple experimental setup. The first application of SBI for virtual histology has been demonstrated recently [43,44]. Here we demonstrate the potential of SBI for retrieving quantitative high-resolution data for virtual histology of the human cerebellum. We also assess the potential benefits of the dark-field modality for extracting unresolved cell architecture in the cerebellar cortex layers.

2.   Materials and methods

2.1.   Sample preparation

Post-mortem specimens of a human cerebellum were collected from a donated brain at the Department of Neuropathology, Universitätsspital Basel, Switzerland. The specimens were fixed in 4% histological-grade buffered formalin, dehydrated in ethanol, transferred to xylene and embedded in paraffin. A metal punch was used to extract two cylinders from the paraffin blocks, one with 1.4 mm and one with 4 mm diameter. All procedures were conducted in accordance with the Declaration of Helsinki and were approved by the ethics committee of northwestern Switzerland (Ethikkommission Nordwestschweiz).

2.2.   Experimental setup

The experiment was performed at the beamline ID19 of the European Synchrotron Radiation Facility, with the setup schematically shown in Fig. 1. To visualize the tissue structure at different length scales, the specimens were scanned at two different effective pixel sizes and photon energies. The configurations used for this experiment, one at medium spatial resolution (MR) with a larger field of view, and a second one at higher spatial resolution (HR), but with a smaller field of view, are described in the following.
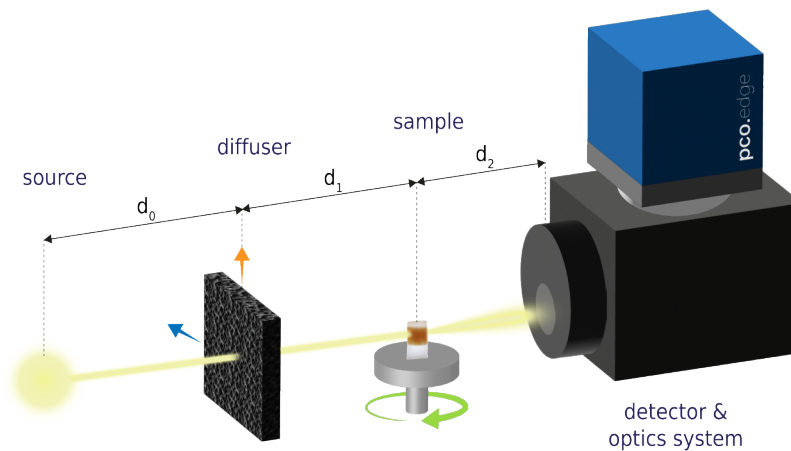

Fig. 1. Experimental setup at the imaging beamline ID19, ESRF (Grenoble, France). Synchrotron radiation from an undulator insertion device is modulated by a diffuser before traversing the sample and finally reaching the detector. The diffuser is used to mark the wavefront, and distortions of the reference speckle pattern introduced by the sample are used to disentangle the different signals—attenuation, diffraction, and small-angle scattering.

An X-ray beam with a narrow energy spectrum and a peak energy of 26.5 keV was used for the MR setup. This was obtained with the U13 single-harmonic undulator (gap: 12.0 mm) in combination with a 1.4 mm-thick diamond exit window and 5.6 mm aluminum filter. The near-field speckle pattern was created by two layers of P800 sandpaper (average grit size 21.8 µm [45]), fixed on a two-axis translation stage for stepping in the plane transverse to the beam direction. The sample was mounted on a tomographic stage located d_1 = 72.5 cm downstream of the diffuser, and the detection system was placed d_2 = 45.0 cm downstream of the sample. The imaging detector consisted of a pco.edge 5.5 sCMOS camera (PCO AG, Kelheim, Germany) with 2560×2160 px coupled to a 2.1× magnification optics system, comprising two Hasselblad lenses (Hasselblad, Gothenburg, Sweden) in tandem configuration with a numerical aperture of 0.17 and a scintillation screen [250 µm-thick cerium-doped lutetium aluminum garnet (LuAG:Ce)].

The effective pixel size of this system was $p_{\text{eff}} = 3.1\,\mu m$. This setup was used for imaging the cerebellum sample with 4 mm diameter.

Acquisition of the sample images was performed in tomographic mode by recording 1801 projections at equidistant viewing angles over 180 degrees of sample rotation. This was repeated for $N = 20$ positions of the phase modulator, which was scanned along a spiral trajectory to avoid grid-like image artifacts between different diffuser steps and prevent erroneous speckle-tracking effects. A set of 20 dark images (i.e., without the beam on the camera) were taken before the entire scan and averaged. The flatfield was estimated by averaging 40 frames taken without the sample and diffuser in the beam. For each diffuser position, and before each of the tomographic scans, a set of 20 reference images was recorded with the diffuser, but without the sample in the beam, which were averaged to obtain a single reference image for each diffuser position. The exposure time per frame was 50 ms, resulting in a total scan time of 46 min.

The HR setup was employed to image the smaller sample (1.4 mm diameter), prompting the use of a lower X-ray energy. The U17 single-harmonic undulator (gap: 11.52 mm) was used without additional filtration. This resulted in a detected spectrum with an average photon energy of 18 keV. The basic components of the experimental arrangement (i.e., camera, microscope, motors) were the same as for the MR setup. However, an objective lens with higher magnification (10×) was used in combination with a 10 μm-thick europium-doped gadolinium aluminum garnet (GGG:Eu) scintillation screen. This yielded an effective pixel size of $p_{\text{eff}} = 0.65\,\mu m$. Finer sandpaper (five layers of P5000, 5 μm grit size [45]) was used to match the near-field speckle size to the higher spatial resolution of the imaging system. The diffuser-sample distance for this setup was $d_1 = 52.5$ cm and the sample-detector distance was $d_2 = 8.5$ cm. For both scans, the source-diffuser distance was roughly $d_0 \approx 145$ m. The data acquisition scheme and parameters were similar to the ones used in the MR setup. However, for the HR measurements, a larger number of projections (2401) was collected for each diffuser step. The same exposure time per frame was used (50 ms), and the total acquisition time was 60 min. The main experimental parameters for the two setups are summarised in Table 1. Additionally, tomography scans without the diffuser in the beam, but otherwise identical acquisition parameters, were taken for both the MR and HR configurations.

Table 1. Experimental parameters for the two tomographic SBI acquisitions.

	MR	HR
Photon energy	26.5 keV	18 keV
Effective pixel size p_{eff}	3.1 μm	0.65 μm
Diffuser-sample distance d_1	72.5 cm	52.5 cm
Sample-detector distance d_2	45.0 cm	8.5 cm
Diffuser	2× P800	5× P5000
Number of diffuser steps N	20	20
Number of projections per step	1801	2401
Acquisition time	46 min	60 min

2.3. Data analysis

The reconstruction of the three-dimensional volumes from the collected raw data was identical for the MR and HR datasets. Initially, all sample images (with sample and diffuser) and reference images (only diffuser) were dark- and flatfield-corrected. Each frame was also normalized by the electron beam current of the storage ring. Dead and bright pixels in the corrected frames were removed by replacing them with the median of their neighbors.

Subsequently, the sets of 20 sample frames recorded at the same tomographic angle but different diffuser positions, as well as the 20 reference frames recorded at matching diffuser positions were processed using UMPA [34,35], after correcting for diffuser drift between reference and sample measurements. This yielded, for each tomographic angle of the sample, the transmission, dark-field and refraction angle signals along two orthogonal directions (see Fig. 2 for one example projection).
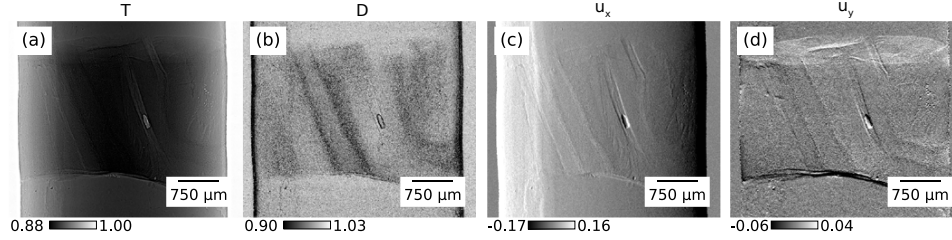

Fig. 2. Signals retrieved with UMPA for one example projection of the MR dataset. **(a)** Transmittance T, **(b)** dark-field D, and the differential-phase signals in the **(c)** horizontal (u_x) and **(d)** vertical direction (u_y); u_x and u_y are given in pixels.

For the MR and HR datasets, an analysis window size of 3×3 px was chosen for the UMPA algorithm, as a compromise between desired spatial resolution and noise level in the final images [34]. In addition, a reconstruction of the MR dataset with a bigger UMPA analysis window of 41×41 px was used to retrieve the dark-field volume. Making use of the small-angle approximation, the horizontal and vertical differential-phase signals $u_{x,y}$ were converted to refraction angles using the relation

$$\alpha_x = \frac{u_x}{d_2} = \frac{\partial}{\partial x} \int \delta(z)\,dz\,, \qquad \alpha_y = \frac{u_y}{d_2} = \frac{\partial}{\partial y} \int \delta(z)\,dz\,, \tag{1}$$

where $\alpha_{x,y}$ are the horizontal and vertical refraction angles, d_2 is the sample-detector propagation distance in multiples of pixel size, and $\int \delta\,dz$ is the integral of the real part of the refractive index δ along the ray path through the object.

Quantitative phase images can be obtained from the horizontal and vertical differential-phase images using the Fourier phase integration routine described in [46]. After phase integration, a 2D polynomial of second order was fitted to the background areas to remove residual low-frequency artifacts. The tomographic reconstructions from the phase, transmittance and dark-field projections were performed by applying a conventional filtered back-projection algorithm [47] using the ASTRA toolbox [48,49]. To reduce ring artifacts in the tomographic slices (originating mainly from scintillator defects, noise, beam instabilities and estimation biases inherent in the UMPA algorithm [35]), a low-pass Butterworth filter was applied to the sinogram of each slice prior to the filtered back-projection step. The resulting phase volumes show the decrement δ of the real part of the sample's refractive index $n = 1 - \delta + i\beta$. From δ we can retrieve the electron density distribution ρ_e using

$$\delta = \frac{2\pi\rho_e r_0}{k^2}\,, \tag{2}$$

where r_0 is the classical electron radius and $k = 2\pi/\lambda$ is the wave number. The refractive index's imaginary part β is related to the linear attenuation coefficient μ and the transmittance signal through the Beer-Lambert law [50] via

$$T = \frac{I}{I_0} = e^{-\int \mu(z)\,dz} = e^{\int 2k\beta(z)\,dz}\,. \tag{3}$$

Finally, the dark-field signal, which accounts for the reduction in visibility caused by small-angle scattering, can be treated similarly to attenuation, and is related to the linear diffusion

coefficient ε [51]:

$$D = \frac{V}{V_0} = e^{-\int \varepsilon(z)\,dz} \ .\tag{4}$$

The HR and MR datasets without a diffuser were processed with the Transport-of-Intensity-homogeneous-sample (TIE-Hom) algorithm [14], which assumes a constant value of $\gamma = \delta/\beta$ for the entire sample. Here we calculate γ with an approach for multi-material systems [52] via $\gamma = (\delta_{\text{brain}} - \delta_{\text{wax}})/(\beta_{\text{brain}} - \beta_{\text{wax}})$. Using tabulated values of δ and β for paraffin wax and brain [53], we obtain a value of $\gamma = 302.5$.

3. Results

3.1. *Speckle pattern characterization*

Figure 3(a) and (b) show two speckle patterns recorded with the MR and HR setups, along with zoomed insets. We note that the HR speckle pattern exhibits a broader intensity distribution [see histogram in Fig. 3(c)] and a larger mean speckle size in pixels compared to the MR setup.
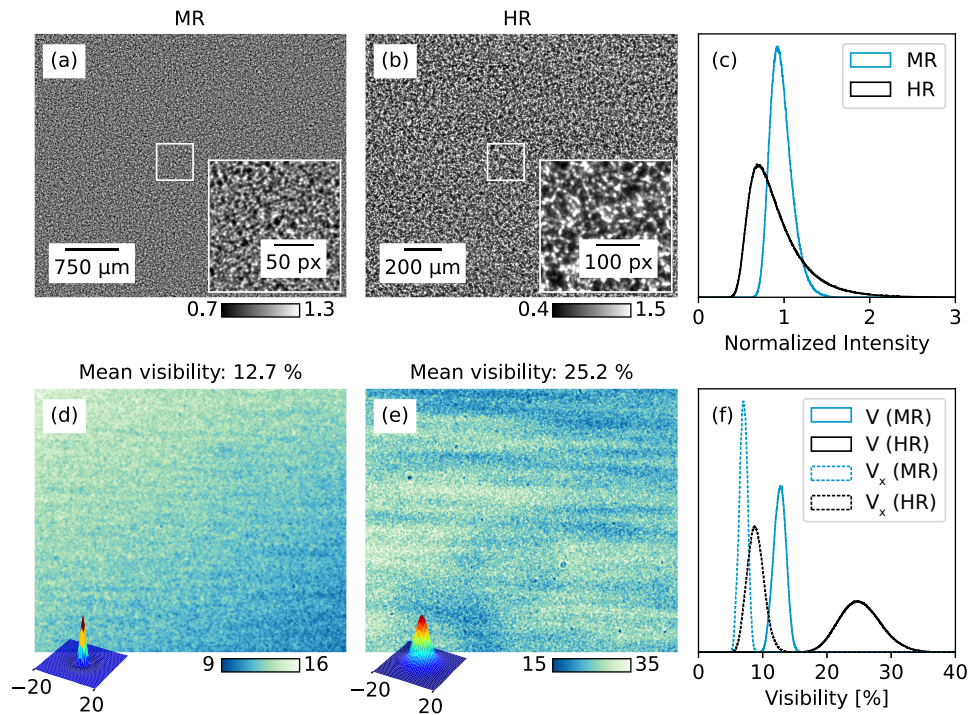

Fig. 3. Speckle characterization and visibility analysis. **(a), (b)** Speckle pattern for the MR and HR setups, with insets of a 166×166 px and 300×300 px region of interest, respectively. **(c)** Normalized intensity distributions of **(a)** and **(b)**. **(d), (e)** show maps of visibility V and 3D representation of the speckle pattern autocorrelation (FWHM$_{\text{MR}}$ = 3.3 px vs. FWHM$_{\text{HR}}$ = 10.1 px). **(f)** Visibility distribution for the two setups.

The mean speckle size in the observation plane can be quantified by evaluating the 2D autocorrelation function of a reference image, and evaluating the width (full width at half maximum, FWHM) of its radial profile. A three-dimensional representation of the speckle size distribution is shown in the insets of Fig. 3(d) and (e), yielding a value of 3.3 px (10.2 μm) and 10.1 px (6.6 μm) for the MR and HR setups, respectively.

The quality of the reconstructions obtained with SBI is related to the properties of the recorded near-field speckle pattern. In particular, the visibility of the near-field speckle pattern can give an indication of the technique's performance for a given setup configuration. This quantity has previously been calculated in different ways [54,55]. Here we adopt the definitions:

$$V = \frac{\sqrt{\frac{1}{N}\sum \sigma_n(I)^2}}{\bar{I}} = \frac{\sqrt{\frac{1}{N}\sum\left(\bar{I}_n^2 - \bar{I}_n^2\right)}}{\bar{I}} \ , \ V_x = \frac{\sqrt{\frac{1}{N}\sum\left|\frac{\partial I_n}{\partial x}\right|^2}}{\bar{I}} \ , \ V_y = \frac{\sqrt{\frac{1}{N}\sum\left|\frac{\partial I_n}{\partial y}\right|^2}}{\bar{I}} \ , \quad (5)$$

where $\sigma_n(I)$ is the standard deviation of the reference image I_n (at diffuser step n) and $\bar{I}$ is the mean value of I, obtained by using a Gaussian filter with a kernel diameter corresponding to the used analysis window in UMPA. Besides the standard-deviation-based visibility metric V, the gradient-based visibility metrics $V_{x,y}$ can be used. These take a potential anisotropy of the speckle pattern into account and are related to noise levels in the differential-phase images $u_{x,y}$ [54].

The visibility maps V for the two setups were determined over the entire field of view (FOV), as shown in Fig. 3(d) and (e). We note that the visibility is not spatially homogeneous throughout the FOV and that the mean values are 12.7% and 25.2% for the MR and HR setup, respectively. Furthermore, in Fig. 3(f) we provide histograms of both visibility V, and gradient-based visibility in the horizontal direction V_x, with a mean value of 7.0% for the MR and 8.9% for the HR configurations, obtained from Eq. (5). Similar distribution shapes and values were estimated for the gradient in the vertical direction, 7.2% and 8.7%, respectively (not shown).

Examples of a pair of horizontal and vertical refraction angle images obtained with UMPA are shown in Fig. 4 for both setups. The standard deviation measured in a background region gives an indication of the setups' sensitivities for measuring the refraction angles. The results obtained in an ROI of 50×50 px, for multiple projections, are reported in Table 2, indicating a higher angular sensitivity of the MR setup, even though the HR setup exhibits higher visibility in Fig. 3. It must be noted that an increase in the sensitivity to refraction typically also leads to an increased sensitivity to experimental imperfections. Mechanical vibrations and variations in source properties lead to changes in speckle pattern shape, which are erroneously attributed to the sample and appear as image artifacts. We found that longer propagation distance, higher visibility, and smaller pixel size all tend to increase the sensitivity of an SBI setup to such disturbances. In particular, we here find that this susceptibility to disturbances can effectively worsen angular sensitivity when an improvement should be expected.
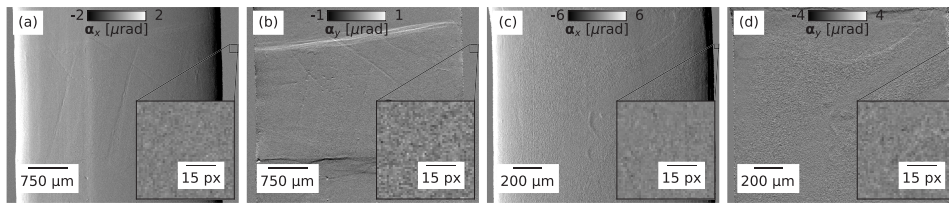

Fig. 4. Example projection of horizontal (α_x) and vertical (α_y) refraction angles from the MR dataset (**a**), (**b**) and the HR dataset (**c**), (**d**). The differential-phase signal from UMPA has been bias-corrected before the analysis, in order to reduce the amount of estimation bias-induced noise. The refraction angles were calculated for propagation distances of $d_{2,\mathrm{MR}} = 45.0\,\mathrm{cm}$ and $d_{2,\mathrm{HR}} = 8.5\,\mathrm{cm}$. Insets show the 50×50 px ROIs used for the calculation of angular sensitivity.

**Table 2. Angular sensitivity of
horizontal (α_x) and vertical (α_y)
differential-phase data from the MR and
HR scans.[a]**

	σ_{α_x} [nrad]	σ_{α_y} [nrad]
MR	147	127
HR	336	328

[a]The sensitivity is estimated by measuring the
standard deviation in an empty background region
(see insets in Fig. 4). Refraction angles were
obtained from the UMPA differential-phase signals
according to Eq. (1).

3.2. Multi-modal cerebellum volumes at medium and high resolution

UMPA allows the simultaneous retrieval of transmittance, refraction and small-angle scattering
information. Moreover, UMPA is flexible in reconstruction sensitivity; spatial resolution can be
traded for increased SNR [34] based on the sample and scientific question. The different signals
retrieved from the speckle-based and propagation-based datasets of the cerebellum sample in the
MR setup are shown in Fig. 5.

Figure 5(a) shows a map of linear attenuation coefficients μ reconstructed from the transmittance
data retrieved with UMPA. It exhibits edge-enhancement effects due to free-space propagation
and the source's high coherence. Hence, the retrieved signal is not pure attenuation; second-order
phase effects are still coupled to the result. This makes the attenuation data obtained with UMPA
suitable for phase retrieval with methods derived for PBI. Using the same value of $\gamma = 302.5$,
both the transmittance data from UMPA (using a 3×3 px analysis window), and the PBI datasets
were processed with the TIE-Hom filter, yielding very similar results. A tomographic slice of the
processed PBI dataset from the MR setup is shown in Fig. 5(b). However, with this method the
estimated phase values are not quantitative; the method is only exact for objects composed of a
single material, and requires prior knowledge about material composition. UMPA, on the other
hand, is able to interpret differential-phase information quantitatively, as shown in Fig. 5(c).

Finally, Fig. 5(d) shows the dark-field channel. This dataset has a considerably lower resolution
than the phase or attenuation channels because it was reconstructed with a much larger UMPA
analysis window (41×41 px, versus the 3×3 px analysis window used for the other channels).
This effectively simulates a setup with a larger pixel size. The use of a larger analysis window was
necessary since dark-field tomograms with smaller analysis windows (up to 11×11 px) exhibited
very high noise levels. While it is well known that dark-field tomography data is often quite noisy,
we think that this is especially pronounced for high-resolution dark-field data: since a voxel in a
high-resolution dataset contains only few scattering features (e.g., particles or interfaces), there is
a high variability of dark-field activity from one voxel to the next. At lower resolutions, this effect
is less pronounced because the number of contributing interfaces is much larger. To somewhat
quantify this: given a constant average density of cells, it is reasonable to assume a Poissonian
distribution for the number of cells in a voxel. The relative standard deviation of this quantity
then scales with $\lambda^{-1/2}$, where λ is the average number of cells per voxel, demonstrating that this
variability decreases with increasing voxel size.

This means that both "true" noise and structural noise are present in high-resolution dark-field
images. This makes the evaluation of spatial resolution in such images difficult. For the
measurements shown here, we have simply chosen the analysis window size large enough
(41×41 px) that both types of noise become negligible. We determined a spatial resolution of
68.3 µm for this setting, comparable to that of the UMPA phase tomograms with the same analysis
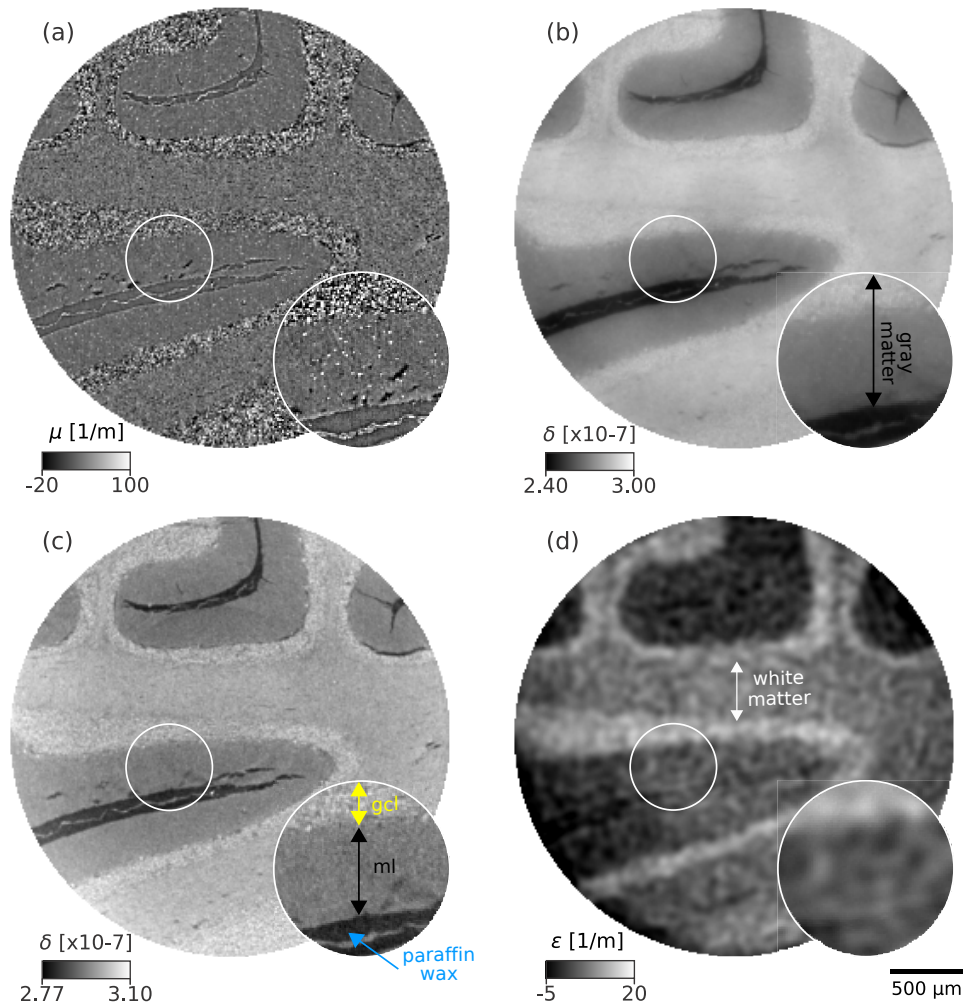window size. This is likely not the highest possible resolution achievable for the dark-field

Fig. 5. Tomographic reconstruction of the four modalities retrieved in the MR scan: **(a)** linear attenuation coefficient μ, retrieved from UMPA transmittance projections, **(b)** index of refraction decrement δ from the PBI scan (projections with no diffuser), **(c)** δ retrieved from UMPA differential-phase data, and **(d)** linear diffusion coefficient ε retrieved from UMPA dark-field data. Insets show a region highlighting contrast differences between paraffin wax, molecular layer (ml), and granular cell layer (gcl).

modality in this dataset, but a more precise analysis at lower analysis window sizes would require the ability to distinguish photon noise and structural noise. This might be achieved in future works by performing the same measurement several times and comparing the results: structural noise should be identical for all measurements, while true noise would change.

Additionally, the scattering structures are not perfectly isotropic, meaning that the dark-field signal generated by a voxel may vary with the tomographic angle, leading to additional uncertainties. We believe that this effect is also less pronounced at lower resolutions due to averaging effects.

The dark-field signal magnitude varies considerably between the different cellular layers: the granular layer generates the strongest dark-field signal, followed by the white matter, and finally the molecular layer generates the weakest signal. Molecular layer and paraffin are nearly indistinguishable. As will be discussed below, the signal level difference between the granular and molecular layers correlates well with the difference in the cell density between these layers, as identified in the HR phase dataset.

3.2.1.   Features in high- and medium-resolution phase-contrast tomograms

While the HR scan allows for the visualization of individual neurons, the MR scan provides a general picture of the different tissue components of the cerebellum. Slices through the tomographic reconstruction of the human cerebellum obtained with the HR setup are shown in Fig. 6, whereas the bigger sample scanned in the MR setup is shown in Fig. 7. The three layers of the cerebellar cortex can be easily identified both at high and medium resolution. The high contrast of the phase volumes allows for the immediate differentiation of gray and white matter, as well as the separation of the gray matter's molecular and granular cell layer. The distinction between the two latter layers, however, is more evident in the dark-field volume.

In addition to a much smaller number of interneurons, granule cells are tightly packed together in the granular cell layer. Although certain clusters of granule cells can be seen in the molecular layer of the MR volume, their contrast is limited by the spatial resolution, and they are easier to see in the HR volume, given their mean cell body size of 5–8 μm [56]. The Purkinje cell layer is a narrow zone that contains only the cell bodies of Purkinje cells located between the granular layer and the molecular layer. The molecular layer, on the other hand, is the cerebellar cortex's outermost layer, containing stellate cells and basket cells, among others. Both stellate and basket cells form synapses on the dendrites of Purkinje cells [see Fig. 6(d)]. Thin axons leave the Purkinje cell base, cross the granular cell layer, become myelinated, and enter the white matter [56]. Purkinje cells are a type of neuron found in the cerebellum, known for their large size and distinctive spherical-shaped bodies. Their size can vary, depending on various factors such as age, sex, and health status. They reach diameters of about 10–70 μm and are packed into a narrow layer perpendicular to the cerebellar folds [56]. The structural arrangement of cells in the brain has been the subject of several research studies since they are crucial to the neural circuit [57,58].

At present, cell visualization relies primarily on two-dimensional techniques like traditional histology and light microscopy [7,59,60], which require sectioning and are usually limited to smaller samples. In our case however, cells can be easily distinguished in the phase-contrast volumes. Moreover, other virtual histology studies (e.g., [28,61]) require direct cell resolution, complex segmentation and analysis procedures to gain information about the cytoarchitecture of the cerebellar cortex. As an alternative, dark-field tomography appears to be able to provide similar information without the need of directly resolving the single structures (see Fig. 7). Due to the lower resolution requirements of the dark-field modality, this may be feasible for considerably larger samples.
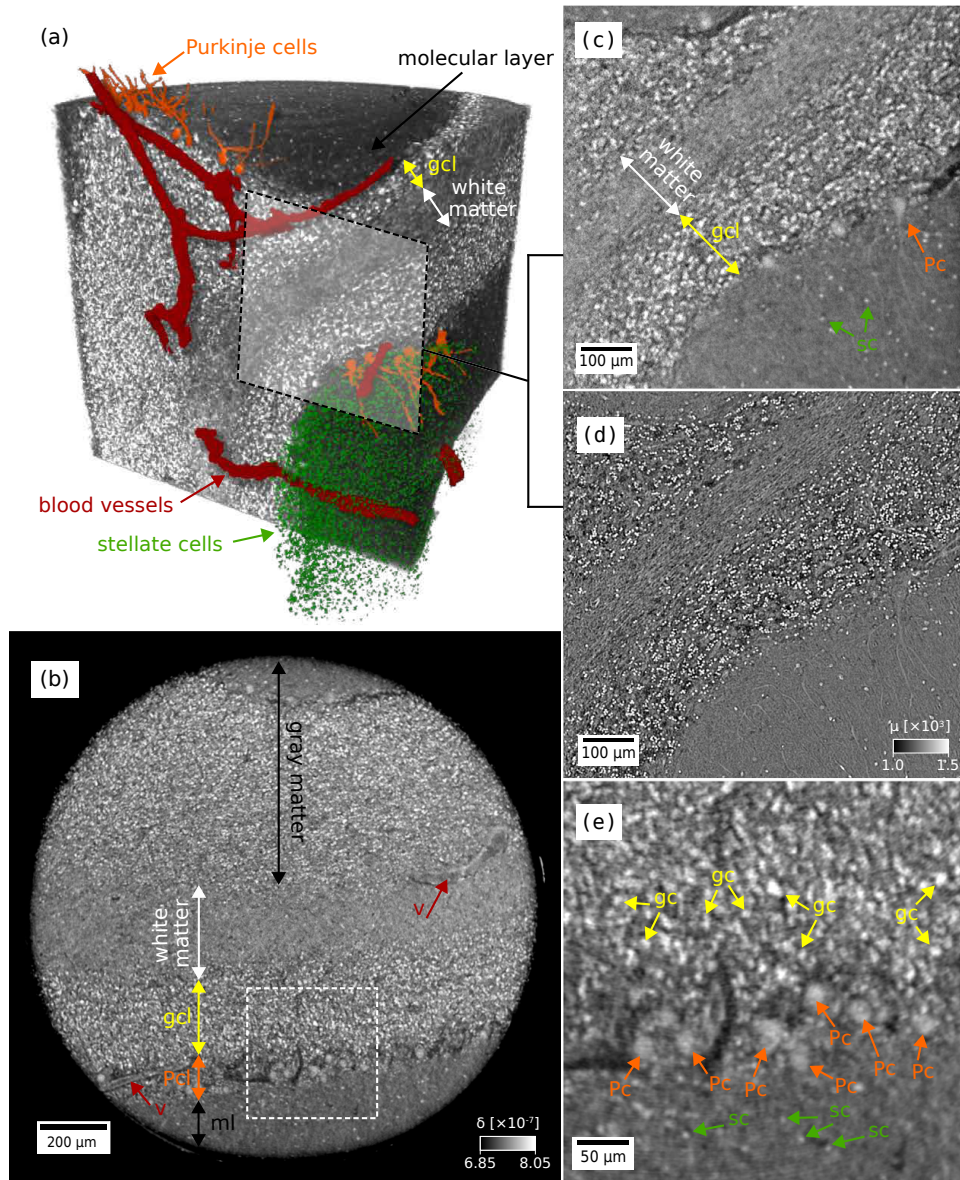
Fig. 6. Phase tomogram of the human cerebellum at higher spatial resolution. **(a)** 3D rendering of the volume with some segmented features. **(b)** Transverse slice. Gray and white matter, as well as the molecular layer (ml), granular cell layer (gcl) and Purkinje cell layer (Pcl) can be distinguished. Large blood vessels (v) are also visible. Panels **(c)** and **(d)** show the same highlighted detail in **(a)** for the phase and the attenuation volumes. Purkinje cells (Pc) and stellate cells (sc) in the molecular layer and the granule cells (gc) in the granular cell layer can be easily distinguished. Synapses joining Pc and sc are better visualized in the attenuation volume, whereas cell bodies have higher contrast in the phase volume. **(e)** ROI of the slice in panel **(b)** at the transition zones of the gcl, Pcl and ml. The nuclei (white dots) of the Purkinje cells can be seen.
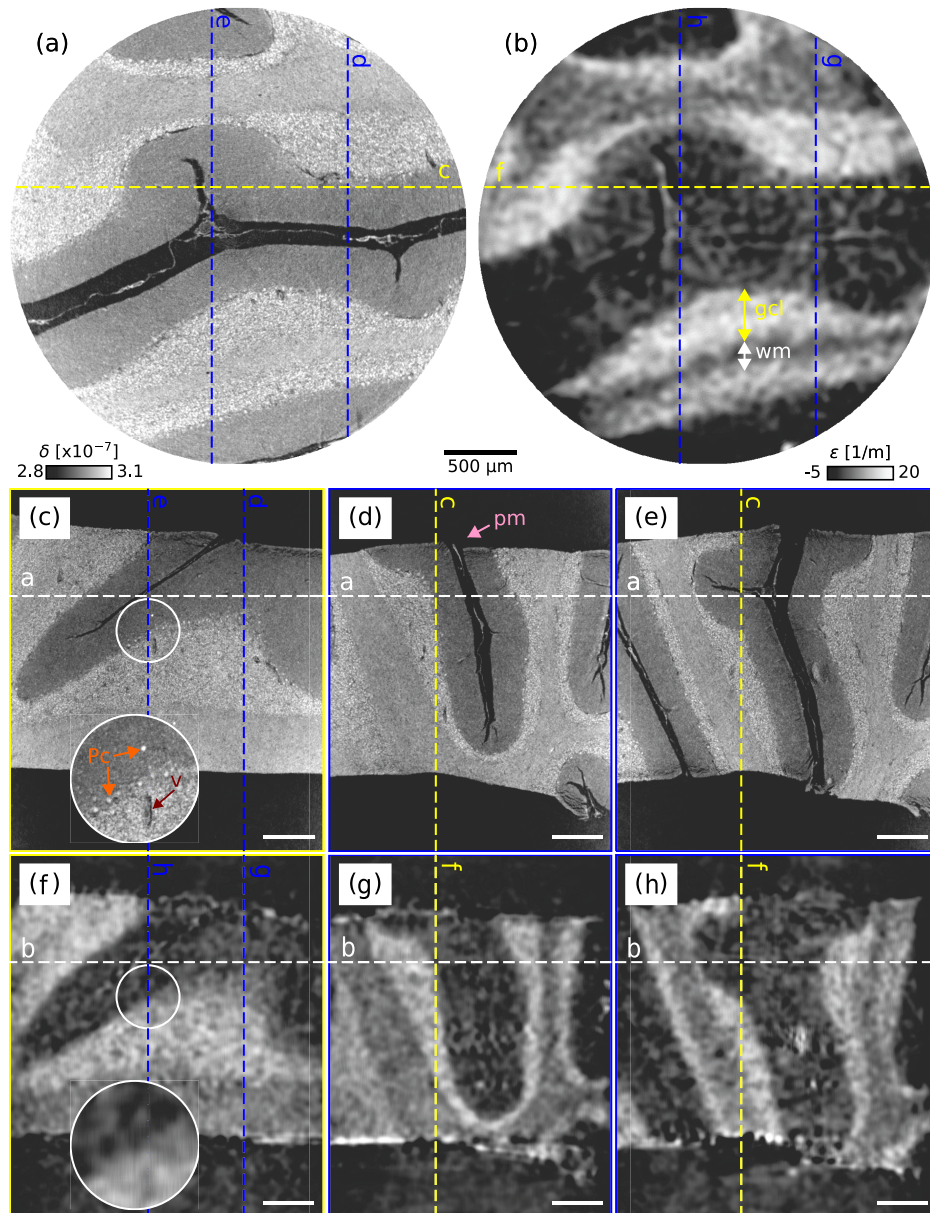
Fig. 7. Phase and dark-field volumes of the human cerebellum acquired at the MR setup. **(a)**,**(b)** Transverse phase and dark-field slice at the same height in the volumes. Different layers in the cerebellar tissue can be distinguished in both. Dark-field shows an increased contrast between the granular cell layer (gcl) and white matter (wm). **(c)** Sagittal slice with a zoomed inset with arrows pointing at a blood vessel (v) and some Purkinje cells (Pc), which appear as bright spots between the molecular layer and the gcl in the phase volume. **(d)**,**(e)** Coronal slices in the phase volume show paraffin infiltration between the cerebellar folds, emphasizing the pia mater (pm), which is the inner membrane enclosing the brain. **(f)**-**(h)** show matching slices through the dark-field volume. The scale bar in **(c)**-**(h)** is 500 µm.

3.2.2.   Relation between dark-field signal and cerebellar microstructures

By analyzing the small-angle scattering of incident X-rays, the dark-field signal can describe the distribution (and orientation [62,63]) of microscopic features within the sample. The granule cell layer is densely packed with granule cells, whereas stellate cells and basket cells, among others, can be found sparsely in the molecular layer, with diameters in the 6–12 μm range [56] (see Fig. 8). White matter hosts axon bundles and fibers that allow the neurons in the cerebellum to communicate with the central nervous system [56]. Different scattering signals are generated by these three layers as a result of a change in electron density, cell size, and cell density.
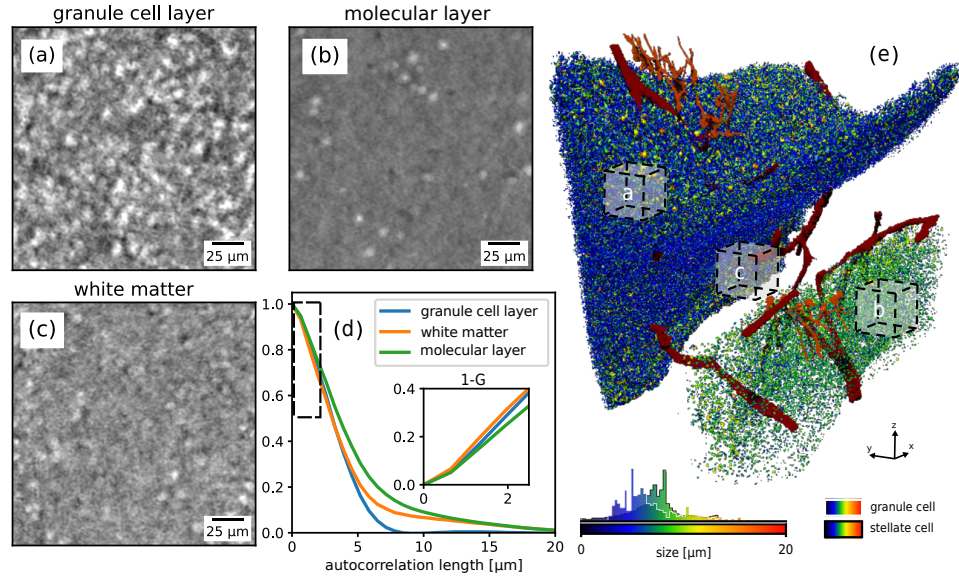

Fig. 8. Cell size distribution and autocorrelation analysis. **(a)**-**(c)** show slices in the $300 \times 300 \times 300$ px ROIs in the HR phase volume for different cerebellar layers. **(d)** shows $G(\xi)$, the radial average of the projection of the 3D autocorrelation for the different ROIs. The inset in **(d)** shows $[1 - G(\xi)]$, the relevant quantity for calculating ε, near the system autocorrelation length. **(e)** Segmentation of the granule cells and stellate cells in the molecular layer is color-coded according to cell size and shown in 3D along with some Purkinje cells (orange) and blood vessels (red). Granule and stellate cell size distributions and colormaps are reported under the segmentation. The locations of the three ROIs in panels **(a)**-**(c)** are highlighted in the 3D representation.

We attempted to relate the findings from the dark-field modality in the MR scans to the phase modality in the HR scans, in order to determine a relation between dark-field signal strength and microstructural parameters. We do this by segmenting cell bodies identified in the HR phase volume and characterizing their mean diameter and volume concentration. From this information we then estimate diffusion coefficients, and compare them to the true diffusion coefficients measured by the dark-field modality in the MR scans.

The material-dependent diffusion coefficient in Eq. (4) is given by $\varepsilon = \Sigma \left[1 - G(\xi) \right]$, where Σ is the macroscopic scattering cross section, and $G(\xi)$ is the projection of the real-space correlation function of electron density, as defined, e.g., in [64]. In analogy to neutron scattering theory [51,64], the macroscopic X-ray scattering cross section for spherical particles in a two-phase system is

$$\Sigma = \lambda^2 (\Delta \rho_e)^2 r_0^2 \Phi (1 - \Phi) \zeta, \tag{6}$$

where λ is the wavelength, $\Delta\rho_e$ is the difference in electron density between particles and the surrounding medium, r_0 is the classical electron radius, and Φ is the volume fraction occupied by the particles. ζ depends on the particle shape, here we use $\zeta = 1.5R$ for spherical particles of radius R [64]. $G(\xi)$ is approximated for the three different tissue types by radially averaging the projection of the 3D autocorrelation function of electron density subvolumes, as shown in Fig. 8(d). Note that in the MR setup, the sampled autocorrelation length is around $\xi = \lambda d_2/p \approx$ 2 μm, meaning that variation of particle diameters in this range strongly affects the dark-field signal. For GBI, p would be the period of the grating self-images on the detector [65]. Here we substitute this with speckle size, similar to an approach shown in [66].

We segmented the cells in the granule cell layer and molecular layer in the HR phase reconstruction and, using the "Ray-Tracing Thicknesses" tool in Dragonfly ORS [67], we estimated mean cell size in these two regions. The two cell size distributions are shown in Fig. 8(e), where the cells are color-coded according to their determined size in the 3D representation. No such analysis was performed for the white matter due to the lack of identifiable, segmentable structures.

The volume packing fraction Φ was obtained by counting the segmented voxels in the respective layers. As a result we estimated that 21% and 1% of the corresponding volumes are filled with granule and stellate cells, respectively.

With the measured mean radius of 2.7 μm and 3.7 μm for granule and stellate cells, we obtain macroscopic scattering cross sections of 41.3 m^{-1} and 0.3 m^{-1}, respectively. Because the contribution of $1 - G(\xi)$ to the diffusion coefficient for the granule and stellate cells is almost identical [since the structure sizes in these regions are considerably larger than the sampled autocorrelation length of 2 μm, see inset in Fig. 8(d)], the measured differences in signal strength in the dark-field volume in Fig. 7 probably originate mainly from Σ, in particular due to the difference in the volume fraction of particles. All the measured parameters in the HR phase segmentation are reported in Table 3, along with the estimated diffusion coefficient ε_{est} for the MR scan and the measured $\varepsilon_{\text{meas}}$ in the MR dark-field volume.

Table 3. Cell segmentation parameters for estimating the dark-field signal.[a]

	R [μm]	Φ [%]	$\Delta\rho_e$ [#el./Å^3]	Σ [1/m]	ε_{est} [1/m]	$\varepsilon_{\text{meas}}$ [1/m]
Granule cell layer	2.7	21	0.44	41.3	11.7	9.8
Molecular layer	3.7	1	0.13	0.3	0.06	1.0
White matter	n.a.	n.a.	0.25	n.a.	n.a.	5.7

[a]R is the mean cell radius from segmentation, Φ the volume fraction occupied by cells, $\Delta\rho_e$ the difference in electron density between cells and surrounding medium, and Σ the macroscopic scattering cross section (see Eq. (6)). ε_{est} shows the estimated linear diffusion coefficient for the MR scan using the evaluated parameters from the HR scan, whereas $\varepsilon_{\text{meas}}$ is the measured dark-field signal in the MR volume. Discrepancies between the two values might originate from segmentation precision and resolution limitations. Our segmentation considered only neuron bodies, excluding axon fibers in the white matter and the intricate synaptic network within the molecular layer.

The quantities ε_{est} and $\varepsilon_{\text{meas}}$ are of the same order of magnitude. Since Eq. (6) combines quantities of extremely different length scales, this suggests that the methodology of the presented approach is correct. However, there is nonetheless a moderate discrepancy between ε_{est} and $\varepsilon_{\text{meas}}$ (a factor of 1.2, or 15, respectively). We believe that this is mainly due to the used approach being too simple. The segmentation step, combined with the two-phase model of Eq. (6) implicitly assumes that any electron density fluctuations inside the cell bodies or the surrounding medium are negligible. This may be a poor approximation especially for the molecular layer, where the volume fraction number of segmented cell bodies (and thus, their relative contribution to the total scatter signal) is low. Additionally, the average radius R, and thus the diffusion coefficient ε for the granule cell layer, may have been overestimated due to the high cell density, effectively

counting two adjacent cells as a single one. Nonetheless, we can say with reasonable certainty that in this measurement, the volume density Φ of cell bodies is the dominant factor impacting the diffusion coefficient, much more so than the dimensions of the scattering structures (for this setup, and other setups with sampled autocorrelation lengths near 2 μm).

As the diameter of thin axons ($\approx$ 1 μm) is very close to the resolution limit of the HR phase-contrast images, their segmentation was not possible. However, we observe fiber-like structures in the attenuation volume in Fig. 6(d), and Fig. 7 indicates the presence of a substantial dark-field signal in white matter. This implies that the dark-field signal has the potential to reveal finer details within the unresolved microstructure of the cerebellum, i.e., even when structures cannot be identified in the other modalities.

We believe that it is possible to extract quantitative information about such unresolved structures with the dark-field modality. Parameters such as (locally averaged) cell density, cell diameter, or fiber thickness could be extracted, despite not resolving these structures directly. However, we acknowledge that our work does not yet achieve this goal. Doing so requires careful work in measuring the dark-field signal of samples with a very well-defined microstructure, and cross-correlating this with an appropriately chosen forward model, similar to Eq. (6).

3.2.3. Spatial resolution in the phase-contrast datasets

We estimated the spatial resolution of the phase-contrast volumes from UMPA, and PBI phase-contrast volumes obtained by filtering transmittance projections from UMPA. For the MR datasets, we additionally performed this analysis for a range of different UMPA analysis window sizes. The analysis was based on the intersection of the image's Fourier Power Spectrum (FPS) with a noise level, a variation of the method proposed in [68]. The standard deviation of gray values in a region of interest (ROI) of a homogeneous portion of the volume can be considered as the global phase sensitivity, which incorporates both the imaging system and the reconstruction sensitivity. Other than by exposure time and detector noise, this value can be influenced by the reconstruction parameters (UMPA analysis window), beam stability, sandpaper choice and sample motor drifts and vibrations. The obtained value also includes contributions from tomographic reconstruction algorithm filters and post-processing corrections (e.g., ring filter), thus establishing a comprehensive noise baseline. The FPS of an ROI in the tomogram delimited by the white box in Fig. 9 was calculated according to [68] and azimuthally averaged. The result is shown in Fig. 9(c), along with the estimated noise baseline. This procedure was repeated for a number of slices yielding consistent values.

The noise baseline in Fourier space was computed by generating an image of the same size as the ROI, containing uncorrelated Gaussian noise with a standard deviation σ estimated from homogeneous ROIs [yellow boxes in Fig. 9(a)], and calculating the radial average of its FPS. The intersection of the image's FPS with the noise baseline approximately defines the highest spatial frequency that can be resolved, yielding a spatial resolution estimate.

We performed this analysis both for the MR and HR datasets. In order to quantify the impact of the UMPA analysis window size on spatial resolution, reconstruction and resolution estimation of the MR dataset were additionally performed for a wide range of analysis window sizes. These results are listed in Table 4. Other methods like threshold-based edge detection [69] gave similar results, while Fourier Shell Correlation [70] failed to give consistent results for different window sizes, possibly due to the presence of low-frequency artifacts in the phase tomograms.
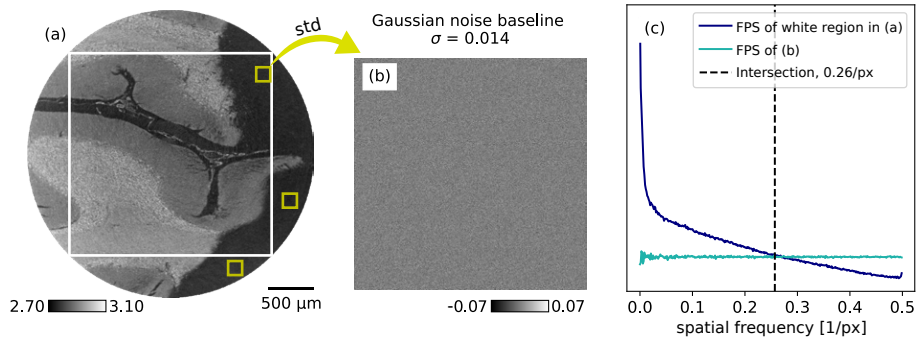
Fig. 9. Spatial resolution estimation in phase tomograms. **(a)** MR phase tomogram slice. Reconstruction sensitivity can be estimated by measuring standard deviation σ in a homogeneous region. Assuming uniformity of the paraffin (dark region in **(a)**), we use the standard deviation inside the yellow regions as a noise estimate. **(b)** Array of same size as white region in **(a)**, containing Gaussian noise with zero mean and standard deviation σ taken from yellow regions in **(a)**. **(c)** Fourier Power Spectum (FPS) of the region highlighted by the white region in **(a)** and that of **(b)**. We define the location f of their intersection as the resolution limit. Given the 3.1 μm pixel size, $f = 0.26/px$ gives a spatial resolution of $1/f = 11.9$ μm. Spatial frequencies under the noise baseline are considered unresolved.

Table 4. Spatial resolution of the phase-contrast reconstructions obtained from the PBI scan without diffuser (TIE-Hom filter proposed in [14]), from the differential phase retrieved in SBI with UMPA, and by filtering the transmittance from UMPA with the TIE-Hom filter.[a]

	HR	MR					
PBI: TIE-Hom phase [μm]	2.9	10.6					
Analysis window size [px]	**3×3**	**3×3**	**5×5**	**7×7**	**9×9**	**11×11**	**41×41**
SBI: UMPA phase [μm]	2.3	11.9	18.6	21.3	25.1	27.9	76.9
SBI: TIE-Hom phase from UMPA transmittance [μm]	3.9	16.7	18.6	24.8	30.6	35.4	111.6

[a]For the MR measurements, spatial resolution was evaluated for a range of UMPA analysis window sizes.

4. Discussion and conclusion

In recent years, advances in technology, neuroscience, and imaging techniques have led to significant progress in the understanding of the brain's structure, function, and role in various neurological and psychological conditions. Interdisciplinary collaborations in fields such as psychology, neuroscience, computer science, and engineering have led to innovative approaches for studying the brain through projects such as The Human Brain Project [71], BRAIN [72], EBRAINS [73], and The Human Organ Atlas [74,75].

In this work, we used SBI to obtain a three-dimensional virtual representation of healthy human cerebellar tissue. Attenuation, phase, and dark-field signals were obtained, providing complementary information for distinguishing different cerebellar layers. The multi-resolution scans at the MR and HR stages proved beneficial for a comprehensive inspection of the cerebellar cortex. The MR scan covered a larger sample area, whereas the HR scan was used to determine the abundance, density, and size of cells in different cerebellar layers.

The direct reconstruction of attenuation data, although offering limited contrast between the cerebellar layers, facilitated cell identification due to edge enhancement at tissue interfaces.

These effects were further utilized for single-material phase retrieval (PBI, second-order phase effects).

Compared to the attenuation data, the phase reconstruction with SBI (first-order phase effects) provided increased contrast between tissues with small density differences and offered good spatial resolution, making it particularly valuable for three-dimensional virtual histology of soft tissue. High-contrast was achieved without the need of staining the sample, as it would be required with conventional microtomography [76]. The images showed that SBI produces results comparable to the well-established PBI method, but additionally provides quantitative electron density values.

The dark-field reconstruction provides information about the unresolved microstructure within the sample. While the MR scan dark-field reconstruction had lower resolution than the HR phase reconstruction, it exhibited good contrast between different cerebellar layers. Our results suggest that the dark-field modality might allow for the assessment of cell density and size, without a need to resolve them directly, thus facilitating the examination of larger samples. However, further investigations and efforts are needed to assess more accurately such quantitative values for complex biological samples.

Additionally, while not explored in this study, the determination of axon fiber directionality could be examined using directional dark-field SBI [62,63] or tensor tomography [77] techniques at microscopic resolutions. The axon fiber connectivity patterns in the brain are traditionally accessed *in vivo* by magnetic resonance imaging (MRI) techniques with a spatial resolution in the millimeter range [78,79]. While more recent techniques employing visible light can yield comparable information at microscopic resolution, they often require sample slicing and can result in non-isotropic volumetric reconstructions [80,81]. Hence, improvements in understanding and analyzing the dark-field signal could contribute to the study of three-dimensional nerve fiber architecture at microscopic resolution, as a prerequisite for a better interpretation and validation of MRI data.

In conclusion, the visualization of the cerebellar cytoarchitecture in three dimensions can provide valuable insights into morphological and cellular details that may be linked to neurological diseases. Contrary to traditional approaches like conventional histology, as well as other visible-light microscopy or electron microscopy techniques, which can suffer from two-dimensional distortions and often require complex sample preparation, SBI overcomes these limitations, enabling non-destructive, multi-modal inspection of the undistorted volume with high sensitivity and resolution. High-resolution three-dimensional virtual inspection of the cerebellar tissue was possible using the attenuation and phase signals. The different cellular layers could also be clearly distinguished in the dark-field modality, despite a considerably lower spatial resolution. We established some correlations between dark-field signal strength and cellular density for two of the three cellular layers. While we cannot yet extract quantitative information from the dark-field modality, our findings indicate potential for extracting cytoarchitectural details from lower-resolution measurements of larger brain samples.

Data availability. Data underlying the results presented in this paper may be obtained from the authors upon request.

References

1. E. D. Louis, R. Babij, M. Lee, *et al.*, "Quantification of cerebellar hemispheric purkinje cell linear density: 32 ET cases versus 16 controls," Mov. Disord. **28**(13), 1854–1859 (2013).

2. R. Babij, M. Lee, E. Cortés, *et al.*, "Purkinje cell axonal anatomy: quantifying morphometric changes in essential tremor versus control brains," Brain **136**(10), 3051–3061 (2013).

3. J. Skefos, C. Cummings, K. Enzer, *et al.*, "Regional Alterations in Purkinje Cell Density in Patients with Autism," PLoS One **9**(2), e81255 (2014).

4. S. Roux, Y. Bailly, and J. L. Bossu, "Regional and sex-dependent alterations in purkinje cell density in the valproate mouse model of autism," NeuroReport **30**(2), 82–88 (2019).

5. T. Wu and M. Hallett, "The cerebellum in Parkinson's disease," Brain **136**(3), 696–709 (2013).

6. Y. Mu and F. H. Gage, "Adult hippocampal neurogenesis and its role in Alzheimer's disease," Mol. Neurodegener. **6**(1), 85 (2011).

7. A. Khimchenko, H. Deyhle, G. Schulz, *et al.*, "Extending two-dimensional histology into the third dimension through conventional micro computed tomography," NeuroImage **139**, 26–36 (2016).

8. A. Li, H. Gong, B. Zhang, *et al.*, "Micro-Optical Sectioning Tomography to Obtain a High-Resolution Atlas of the Mouse Brain," Science **330**(6009), 1404–1408 (2010).

9. W. Pawlina and M. H. Ross, *Histology: A Text and Atlas* (Lippincott Williams and Wilkins, 2018), 8th ed.

10. C. Bikis, G. Rodgers, H. Deyhle, *et al.*, "Sensitivity comparison of absorption and grating-based phase tomography of paraffin-embedded human brain tissue," Appl. Phys. Lett. **114**(8), 083702 (2019).

11. S. W. Wilkins, T. E. Gureyev, D. Gao, *et al.*, "Phase-contrast imaging using polychromatic hard X-rays," Nature **384**(6607), 335–338 (1996).

12. P. Cloetens, R. Barrett, J. Baruchel, *et al.*, "Phase objects in synchrotron radiation hard x-ray imaging," J. Phys. D: Appl. Phys. **29**(1), 133–146 (1996).

13. R. Fitzgerald, "Phase-Sensitive X-Ray Imaging," Phys. Today **53**(7), 23–26 (2000).

14. D. Paganin, S. C. Mayo, T. E. Gureyev, *et al.*, "Simultaneous phase and amplitude extraction from a single defocused image of a homogeneous object," J. Microsc. **206**(1), 33–40 (2002).

15. F. Pfeiffer, M. Bech, O. Bunk, *et al.*, "Hard-x-ray dark-field imaging using a grating interferometer," Nat. Mater. **7**(2), 134–137 (2008).

16. M. Bech, O. Bunk, T. Donath, *et al.*, "Quantitative x-ray dark-field computed tomography," Phys. Med. Biol. **55**(18), 5529–5539 (2010).

17. K. Taphorn, F. De Marco, J. Andrejewski, *et al.*, "Grating-based spectral x-ray dark-field imaging for correlation with structural size measures," Sci. Rep. **10**(1), 13195 (2020).

18. A. Doherty, S. Savvidis, C. Navarrete-León, *et al.*, "Edge-Illumination X-Ray Dark-Field Tomography," Phys. Rev. Appl. **19**(5), 054042 (2023).

19. M. N. Wernick, O. Wirjadi, D. Chapman, *et al.*, "Multiple-image radiography," Phys. Med. Biol. **48**(23), 3875–3895 (2003).

20. L. Rigon, A. Astolfo, F. Arfelli, *et al.*, "Generalized diffraction enhanced imaging: Application to tomography," Eur. J. Radiol. **68**(3), S3–S7 (2008).

21. F. Pfeiffer, T. Weitkamp, O. Bunk, *et al.*, "Phase retrieval and differential phase-contrast imaging with low-brilliance x-ray sources," Nat. Phys. **2**(4), 258–261 (2006).

22. A. Olivo and R. Speller, "A coded-aperture technique allowing x-ray phase contrast imaging with conventional sources," Appl. Phys. Lett. **91**(7), 074106 (2007).

23. S. Bérujon, E. Ziegler, R. Cerbino, *et al.*, "Two-Dimensional X-Ray Beam Phase Sensing," Phys. Rev. Lett. **108**(15), 158102 (2012).

24. K. S. Morgan, D. M. Paganin, and K. K. W. Siu, "X-ray phase imaging with a paper analyzer," Appl. Phys. Lett. **100**(12), 124102 (2012).

25. I. Zanette, T. Zhou, A. Burvall, *et al.*, "Speckle-Based X-Ray Phase-Contrast and Dark-Field Imaging with a Laboratory Source," Phys. Rev. Lett. **112**(25), 253903 (2014).

26. G. Schulz, T. Weitkamp, I. Zanette, *et al.*, "High-resolution tomographic imaging of a human cerebellum: comparison of absorption and grating-based phase contrast," Phys. Med. Biol. **7**(53), 1665–1676 (2010).

27. G. Schulz, C. Waschkies, F. Pfeiffer, *et al.*, "Multimodal imaging of human cerebellum - merging X-ray phase microtomography, magnetic resonance microscopy and histology," Sci. Rep. **2**(1), 826 (2012).

28. M. Töpperwien, F. van der Meer, C. Stadelmann, *et al.*, "Three-dimensional virtual histology of human cerebellum by X-ray phase-contrast tomography," Proc. Natl. Acad. Sci. **115**(27), 6940–6945 (2018).

29. M. Töpperwien, F. van der Meer, C. Stadelmann, *et al.*, "Correlative x-ray phase-contrast tomography and histology of human brain tissue affected by alzheimer's disease," NeuroImage **210**, 116523 (2020).

30. M. Chourrout, C. Sandt, T. Weitkamp, *et al.*, "Virtual histology of Alzheimer's Disease: Biometal entrapment within amyloid-β plaques allows for detection via X-ray phase-contrast imaging," Acta Biomaterialia (2023). In press.

31. S. E. Hieber, C. Bikis, A. Khimchenko, *et al.*, "Tomographic brain imaging with nucleolar detail and automatic cell counting," Sci. Rep. **6**(1), 32156 (2016).

32. A. Khimchenko, C. Bikis, A. Pacureanu, *et al.*, "Hard X-Ray Nanoholotomography: Large-Scale, Label-Free, 3D Neuroimaging beyond Optical Limit," Adv. Sci. **5**(6), 1700694 (2018).

33. S. Berujon and E. Ziegler, "X-ray Multimodal Tomography Using Speckle-Vector Tracking," Phys. Rev. Appl. **5**(4), 044014 (2016).

34. M.-C. Zdora, P. Thibault, T. Zhou, *et al.*, "X-ray Phase-Contrast Imaging and Metrology through Unified Modulated Pattern Analysis," Phys. Rev. Lett. **118**(20), 203903 (2017).

35. F. De Marco, S. Savatović, R. Smith, *et al.*, "High-speed processing of X-ray wavefront marking data with the Unified Modulated Pattern Analysis (UMPA) model," Opt. Express **31**(1), 635–650 (2023).

36. B. Pan, K. Qian, H. Xie, *et al.*, "Two-dimensional digital image correlation for in-plane displacement and strain measurement: a review," Meas. Sci. Technol. **20**(6), 062001 (2009).

37. D. M. Paganin, H. Labriet, E. Brun, *et al.*, "Single-image geometric-flow x-ray speckle tracking," Phys. Rev. A **98**(5), 053813 (2018).

38. K. M. Pavlov, D. M. Paganin, H. T. Li, *et al.*, "X-ray multi-modal intrinsic-speckle-tracking," J. Opt. **22**(12), 125604 (2020).

39. L. Quénot, H. Rougé-Labriet, S. Bohic, *et al.*, "Implicit tracking approach for x-ray phase-contrast imaging with a random mask and a conventional system," Optica **8**(11), 1412 (2021).

40. S. J. Alloo, K. S. Morgan, D. M. Paganin, *et al.*, "Multimodal intrinsic speckle-tracking (MIST) to extract images of rapidly-varying diffuse x-ray dark-field," Sci. Rep. **13**(1), 5424 (2023).

41. M. Riedel, K. Taphorn, A. Gustschin, *et al.*, "Comparing x-ray phase-contrast imaging using a talbot array illuminator to propagation-based imaging for non-homogeneous biomedical samples," Sci. Rep. **13**(1), 6996 (2023).

42. M. R. Teague, "Deterministic phase retrieval: a Green's function solution," J. Opt. Soc. Am. **73**(11), 1434–1441 (1983).

43. M.-C. Zdora, P. Thibault, W. Kuo, *et al.*, "X-ray phase tomography with near-field speckles for three-dimensional virtual histology," Optica **7**(9), 1221 (2020).

44. M.-C. Zdora, *X-ray Phase-Contrast Imaging Using Near-Field Speckles* (Springer International Publishing, 2021).

45. *Federation of European Producers of Abrasives (2023) FEPA P-grit sizes coated abrasives*. https://www.fepa-abrasives.com/abrasive-products/grains. Accessed July 2023.

46. P. Bon, S. Monneret, and B. Wattellier, "Noniterative boundary-artifact-free wavefront reconstruction from its derivatives," Appl. Opt. **51**(23), 5698 (2012).

47. A. C. Kak and M. Slaney, *Principles of Computerized Tomographic Imaging* (Society for Industrial and Applied Mathematics, 2001).

48. W. van Aarle, W. J. Palenstijn, J. De Beenhouwer, *et al.*, "The ASTRA Toolbox: A platform for advanced algorithm development in electron tomography," Ultramicroscopy **157**, 35–47 (2015).

49. W. van Aarle, W. J. Palenstijn, J. Cant, *et al.*, "Fast and flexible X-ray tomography using the ASTRA toolbox," Opt. Express **24**(22), 25129–25147 (2016).

50. J. Als-Nielsen and D. McMorrow, *Elements of Modern X-ray Physics* (Wiley, 2011), 1st ed.

51. M. Strobl, "General solution for quantitative dark-field contrast imaging with grating interferometers," Sci. Rep. **4**(1), 7243 (2014).

52. L. C. P. Croton, K. S. Morgan, D. M. Paganin, *et al.*, "In situ phase contrast X-ray brain CT," Sci. Rep. **8**(1), 11412 (2018).

53. T. Schoonjans, A. Brunetti, B. Golosio, *et al.*, "The xraylib library for x-ray–matter interactions. recent developments," Spectrochim. Acta, Part B **66**(11-12), 776–784 (2011).

54. T. Zhou, M.-C. Zdora, I. Zanette, *et al.*, "Noise analysis of speckle-based x-ray phase-contrast imaging," Opt. Lett. **41**(23), 5490 (2016).

55. M.-C. Zdora, "State of the Art of X-ray Speckle-Based Phase-Contrast and Dark-Field Imaging," J. Imaging **4**(5), 60 (2018).

56. V. P. Eroschenko, *Atlas of Histology with Functional Correlations* (Wolters Kluwer, 2017), 13th ed.

57. S. Guo, J. Xue, J. Liu, *et al.*, "Smart imaging to empower brain-wide neuroscience at single-cell levels," Brain Inf. **9**(1), 10 (2022).

58. H. Skibbe, M. F. Rachmadi, K. Nakae, *et al.*, "The Brain/MINDS Marmoset Connectivity Resource: An open-access platform for cellular-level tracing and tractography in the primate brain," PLoS Biol. **21**(6), e3002158 (2023).

59. P. Osten and T. W. Margrie, "Mapping brain circuitry with a light microscope," Nat. Methods **10**(6), 515–523 (2013).

60. M. Stefaniuk, E. J. Gualda, M. Pawlowska, *et al.*, "Light-sheet microscopy imaging of a whole cleared rat brain with Thy1-GFP transgene," Sci. Rep. **6**(1), 28209 (2016).

61. J. Frost, B. Schmitzer, M. Töpperwien, *et al.*, "3d Virtual Histology Reveals Pathological Alterations of Cerebellar Granule Cells in Multiple Sclerosis," Neuroscience **520**, 18–38 (2023).

62. K. M. Pavlov, D. M. Paganin, K. S. Morgan, *et al.*, "Directional dark-field implicit x-ray speckle tracking using an anisotropic-diffusion Fokker-Planck equation," Phys. Rev. A **104**(5), 053505 (2021).

63. R. Smith, F. De Marco, L. Broche, *et al.*, "X-ray directional dark-field imaging using Unified Modulated Pattern Analysis," PLoS One **17**(8), e0273315 (2022).

64. R. Andersson, L. F. van Heijkamp, I. M. de Schepper, *et al.*, "Analysis of spin-echo small-angle neutron scattering measurements," J. Appl. Crystallogr. **41**(5), 868–885 (2008).

65. S. K. Lynch, V. Pai, J. Auxier, *et al.*, "Interpretation of dark-field contrast and particle-size selectivity in grating interferometers," Appl. Opt. **50**(22), 4310 (2011).

66. S. Meyer, S. Z. Shi, N. Shapira, *et al.*, "Quantitative analysis of speckle-based x-ray dark-field imaging using numerical wave-optics simulations," Sci. Rep. **11**(1), 16113 (2021).

67. *Dragonfly 2020.2 [Computer software]. Object Research Systems (ORS) Inc, Montreal, Canada, 2020*. Software available at http://www.theobjects.com/dragonfly.

68. P. Modregger, D. Lübbert, P. Schäfer, *et al.*, "Spatial resolution in Bragg-magnified X-ray images as determined by Fourier analysis," Phys. Status Solidi A **204**(8), 2746–2752 (2007).

69. A. Gustschin, M. Riedel, K. Taphorn, *et al.*, "High-resolution and sensitivity bi-directional x-ray phase contrast imaging using 2d Talbot array illuminators," Optica **8**(12), 1588–1595 (2021).

70. M. van Heel and M. Schatz, "Fourier shell correlation threshold criteria," J. Struct. Biol. **151**(3), 250–262 (2005).

71. *The Human Brain Project*. https://www.humanbrainproject.eu. Accessed August 2023.

72. *The BRAIN Initiative*. https://braininitiative.nih.gov/. Accessed August 2023.

73. *EBRAINS - A state-of-the-art ecosystem for neuroscience*. https://www.ebrains.eu. Accessed August 2023.

74. *The Human Organ Atlas. ESRF-EBS*. https://human-organ-atlas.esrf.eu. Accessed August 2023.

75. C. L. Walsh, P. Tafforeau, W. L. Wagner, *et al.*, "Imaging intact human organs with local resolution of cellular structures using hierarchical phase-contrast tomography," Nat. Methods **18**(12), 1532–1541 (2021).

76. M. Busse, M. Müller, M. A. Kimm, *et al.*, "Three-dimensional virtual histology enabled through cytoplasm-specific X-ray stain for microscopic and nanoscopic computed tomography," Proc. Natl. Acad. Sci. **115**(10), 2293–2298 (2018).

77. J. Kim, M. Kagias, F. Marone, *et al.*, "X-ray scattering tensor tomography with circular gratings," Appl. Phys. Lett. **116**(13), 134102 (2020).

78. D. S. Tuch, T. G. Reese, M. R. Wiegell, *et al.*, "Diffusion MRI of Complex Neural Architecture," Neuron **40**(5), 885–895 (2003).

79. S. Mori and J. Zhang, "Principles of Diffusion Tensor Imaging and Its Applications to Basic Neuroscience Research," Neuron **51**(5), 527–539 (2006).

80. M. Menzel, J. Reckfort, D. Weigand, *et al.*, "Diattenuation of brain tissue and its impact on 3d polarized light imaging," Biomed. Opt. Express **8**(7), 3163–3197 (2017).

81. M. Menzel, M. Axer, H. D. Raedt, *et al.*, "Toward a High-Resolution Reconstruction of 3D Nerve Fiber Architectures and Crossings in the Brain Using Light Scattering Measurements and Finite-Difference Time-Domain Simulations," Phys. Rev. X **10**(2), 021002 (2020).